Investigation of the relationship between morphology and permeability for open-cell foams using virtual materials testing

Daniel Westhoff[a,*], Jakub Skibinski[b], Ondřej Šedivý[a], Bartlomiej Wysocki[b,c], Tomasz Wejrzanowski[b], Volker Schmidt[a]

[a] *Ulm University, Institute of Stochastics, Helmholtzstr. 18, 89069 Ulm, Germany*
[b] *Warsaw University of Technology, Faculty of Materials Science and Engineering, Woloska 141, 02-507 Warsaw, Poland*
[c] *Materialscare LLC, Zwierzyniecka 10/1, 15-333 Bialystok, Poland*

Abstract

The effect of the morphology of open-cell foam structures on their functional properties is investigated. A stochastic microstructure model is used to generate representative 3D open-cell foam structures, where morphological properties are systematically varied. Subsequently, permeability of these virtual, but realistic microstructures is determined using the finite volume method. This procedure, which is called virtual materials testing, has recently been employed to investigate the effect of the variation of cell sizes on permeability. In the present paper, we introduce a stochastic microstructure model that can be used to generate structures with varying distribution of (open) face sizes between cells. It turns out that this characteristic strongly influences the so-called constrictivity, a measure for bottleneck effects, which, in turn, has a strong impact on the resulting permeability. Moreover, we show how the virtual materials testing approach can be applied to derive empirical formulas between descriptors of 3D morphology and functionality. Additionally, an experimental validation of the simulation results is performed by printing three of the virtual structures using selective laser melting and subsequent experimental measurement of pressure drop, which allows calculation of the permeability using Darcy's law.

*Corresponding author
Email address: daniel.westhoff@uni-ulm.de (Daniel Westhoff)

Keywords: open foam, virtual materials testing, microstructure-property relationship, constrictivity, permeability, coefficient of variation

1. Introduction

Open-cell foams offer a wide range of possible applications, e.g. as filters [1], as materials for heat exchangers [2], or as catalyst supports [3]. For an overview, we refer to [4]. Depending on the application, different functional properties are desirable and the identification of foam structures that optimize functionality is an important goal. It is known that the microstructure of open-cell foams has a strong influence on their functional properties, see, e.g., [5]. There are many experimental studies which investigate this relationship, see, e.g. [6, 7, 8] for the effect of porosities and pore densities on pressure drop in open-cell alumina foams. However, laboratory experiments require huge efforts, which involve manufacturing, tomographic imaging, quantification of structural characteristics and analysis of functional properties.

A way to facilitate the materials design process is to use modeling and simulation. An early approach to express functional properties in a formula by geometric parameters can be found in [9]. There, permeability is considered as a functional property, which is expressed as a function of geometric parameters under certain assumptions of the underlying geometry. To be more precise, the flow phase is assumed to consist of non-intersecting tubes canted at a given angle. It is shown that the function correctly predicts the order of magnitude of permeability also for more complex systems, however, the exact value is misjudged already by a factor of 2 for random lattice networks. Extensions of this work are presented in [10] and [11], where sound absorption properties are related to morphological characteristics. Still, an idealized structure is considered, i.e., a so called unit-cell. This approach neglects more refined morphological properties. An overview on further modeling approaches for thermal conductivity and hydraulic properties in open-cell foams can be found in [12] and [13].

In the present paper, in contrast to analytical models and models for ide-

alized structures, we propose a different approach, which is purely data-driven, where data is gained from simulated, realistic 3D microstructures. The idea is to generate a wide spectrum of virtual, but realistic microstructures, and to analyze functional properties using, e.g., the finite volume method (FVM) or finite element method (FEM), see, e.g., [14]. As, in many materials, different regions in the same piece of material can have slightly different microstructures, which are, however, similar in a statistical sense, stochastic microstructure models are used for generating 3D microstructures as input information for the simulation of functional properties. These models capture the local heterogeneity of the material, but reflect its overall statistical properties, see, e.g., [15, 16]. The whole procedure, which is called virtual materials testing, can then be used to derive relationships between morphological and functional properties, which finally allows one to identify structures with preferable functional properties. This has, e.g., successfully been done in [17] for predicting effective conductivity in materials dedicated to fuel cell applications. While the resulting formulas are not directly deduced by arguments from theoretical physics, the procedure has two main advantages. On the one hand, instead of idealized unit cells, realistic 3D structures are considered, where the stochastic modeling approach ensures that the local randomness of the structure within materials is captured. On the other hand, the formulas that are derived typically lead to a high prediction accuracy [17].

Thus, if a tool is on hand that systematically generates virtual open-cell foam microstructures with varying morphological properties on the computer, numerical simulations can be used to predict the permeability of these virtual materials. A stochastic model based on Laguerre tessellations induced by a random packing of non-overlapping spheres is widely used in literature [18, 19]. A Laguerre tessellation divides the region of interest into a system of convex polytopes. Each polytope is interpreted as a cell of the foam structure, and the edges of each cell are considered as a model of the strut system of open-cell foams. The edges are either dilated to tubes [18] or dilated by spheres with locally varying size to account for the fact that in real microstructures struts are

thicker near the junctions than in their middle parts [20]. A great advantage of the approach via Laguerre tessellations is that it allows for a systematic variation of the cell volume distribution, see e.g. [21]. This allows (in combination with FVM) an investigation of the influence of variations of cell volumes on pressure drop, see [22]. However, it is well known that the performance of functional materials is typically influenced by several morphological characteristics, see, e.g., [17]. The goal of the present paper is to investigate the influence of the coefficient of variation of (open) face sizes (where a 'face' is the surface between two cells). For open-cell foams, the faces play an important role, as the transport paths are passing through them. Note that in [10], the effect of the so-called 'throat size', which is related to the face size, has been investigated based on a single, idealized cell. Here, we consider a realistic 3D system of cells with random variation of cell and face sizes, as they occur in real materials. This allows us to not only investigate the effect of one deterministic face size for all cells in the system, but the variation of face sizes within each structure.

In order to investigate the influence of the distribution of face sizes, a modeling approach for open-cell foams that allows a systematic variation of the face size distribution, while keeping other properties fixed, is needed. The modeling approach via random Laguerre tessellations based on non-overlapping spheres can be extended to systems of overlapping spheres, as the tessellation can be defined in the same manner. This generalization of the modeling approach enlarges the set of possibly generated structures, giving the option to systematically vary other morphological characteristics. In particular, with increasing overlap of spheres, the distribution of face sizes can be modified. Moreover, the stochastic model renders it possible to keep the coefficient of variation of cell volumes almost constant, while varying the coefficient of variation of face sizes. This finally enables us to investigate the influence of the face size distribution on permeability independently of the influence of the cell volume distribution. It turns out that the coefficient of variation of the face sizes is strongly correlated with the so-called constrictivity, a morphological parameter describing bottleneck effects [23]. Subsequently, an analysis of permeability of the simulated

structures is performed using FVM. The results indicate that with increasing coefficient of variation of face sizes, the constrictivity increases, which ultimately leads to an increase in permeability.

An experimental validation of our findings is performed by 3D printing of three of the virtual structures generated by the stochastic model using selective laser melting (SLM) [24] and subsequent experimental analysis of pressure drop. Permeability is then calculated using Darcy's law [25].

The outline of this paper is as follows. In Section 2, the applied methods are introduced. In particular, the stochastic microstructure model is described in detail in Section 2.1, its usage to generate structures with different morphological properties is discussed in Section 2.2, fluid flow simulations via FVM are described in Section 2.3, SLM for printing virtual structures is explained in Section 2.4, and the experimental measurement of pressure drop is described in Section 2.5. In Section 3, an experimental validation of our approach is presented. Then, in Section 4 the results of our investigations are presented and discussed. A comparison to structures with a different morphology of the struts is shown in Section 5. Conclusions are given in Section 6.

2. Methods

2.1. Stochastic microstructure model

As already mentioned above, random Laguerre tessellations based on systems of overlapping spheres are used for the stochastic microstructure model of open-cell foams. A Laguerre tessellation is formally defined as follows. Given a system of marked points $\{(x_i, r_i),\ x_i \in \mathbb{R}^3,\ r_i > 0,\ i \geq 1\}$ in $\mathbb{R}^3$, the 3-dimensional Euclidean space is divided into convex sets, so-called cells $\{c_i,\ i \geq 1\}$, where a point $x \in \mathbb{R}^3$ belongs to the cell $c_i \subseteq \mathbb{R}^3$ if

$$||x_i - x||^2 - r_i^2 \leq ||x_j - x||^2 - r_j^2 \text{ for all } j \neq i. \tag{1}$$

Here, $||a - b||$ denotes the Euclidean distance between two points $a, b \in \mathbb{R}^3$. Intuitively, this means that a point $x \in \mathbb{R}^3$ belongs to the cell c_i induced by x_i,

if its distance to x_i is not larger than to any other x_j, $j \neq i$, where a weighted version of the Euclidean distance is taken as a distance measure. For more details, we refer to [26] and [27].

Note that a system of spheres in $\mathbb{R}^3$ can be considered as a marked point pattern, where the centers of spheres define the coordinates of the points and the radii are considered as their marks. Thus, systems of spheres can be used as generators for Laguerre tessellations. A 2D visualization of generating spheres and the corresponding tessellation can be found in Figure 1(a), where each cell is labeled using the same type of color as its inducing sphere. The struts of a foam structure are then modeled as the dilated edges of the facets of the Laguerre cells. Such a facet between two spheres is shown as a 3D sketch in Figure 1(b) together with the corresponding dilated edges. The Laguerre facet (red area) depicts a face of the open-cell foam structure, through which transport is taking place, while the dilated edges depict the struts. In Figure 1(c) a strut system induced by several spheres is shown.

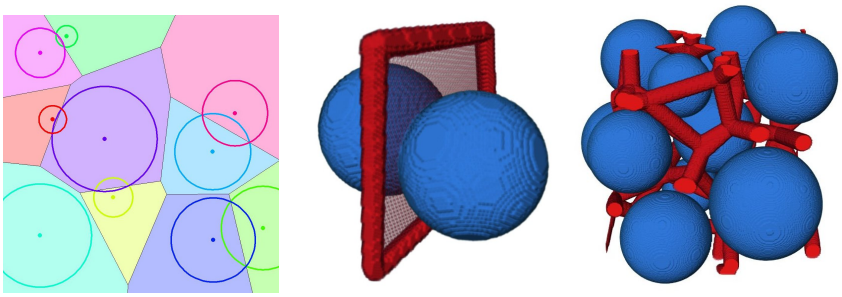

(a) (b) (c)

Figure 1: (a) Laguerre tesellation in 2D induced by a system of overlapping spheres. Cells are labeled using the same type of color as their inducing spheres. (b) 3D view of a Laguerre facet (red area) between two spheres and the corresponding dilated struts (red tubes). Further generating spheres of the tessellation are not shown to enhance visibility. (c) Strut system induced by several spheres.

A well-known algorithm for the generation of non-overlapping spheres is the force-biased algorithm [28, 29]. Based on an initial configuration, it pushes

spheres away from each other until there is no more overlap. This algorithm can be slightly modified to generate systems of overlapping spheres as described in [30]. The idea is as follows.

We consider a bounded sampling window $W \subset \mathbb{R}^3$. The packing density ρ is defined as the volume of all spheres divided by the size of the sampling window. In a first step, the initial configuration of spheres is generated, such that a predefined packing density ρ is achieved, i.e., spheres are thrown at random into the sampling window until the volume of all spheres divided by the volume of the sampling window is equal to ρ. Note that periodic boundary conditions are applied, so no edge correction has to be performed. The radii of the spheres follow some predefined distribution. Such an initial configuration is visualized in Figure 2(a). Then, each sphere is scaled by a so-called core-shell ratio c, where $0 < c \leq 1$. In case $c = 1$, the algorithm described here is identical to the force-biased algorithm for packing of non-overlapping spheres. An example for $c = 0.5$ is shown in Figure 2(b). Then, the force-biased algorithm is applied to the system of scaled spheres. This results in a system of non-overlapping (small) spheres, see Figure 2(c). These small spheres are then scaled back to their original size, i.e., their radii are divided by c. The result is a system of slightly overlapping spheres, see Figure 2(d), where the degree of overlap depends on c, i.e., the smaller c, the higher the degree of overlap. Based on this system of spheres, the corresponding Laguerre tessellation is constructed. The edges of its facets are shown in red color in Figure 2(e). These edges are dilated with some radius $r > 0$ to model the struts of an open-cell foam. The final output of the algorithm is visualized in Figure 2(f). A simulated open-cell foam structure with the same size as considered in all further steps throughout this paper is shown in Figure 3.

Throughout this paper, we choose the packing density to be $\rho = 0.63$, as this gives a good balance between computational feasibility and high volume fraction of spheres. The system of struts is discretized on a voxel grid with 512^3 voxels and a voxel size of approximately 68 µm, i.e., the sampling window W is W=$([0, 35]$ mm$)^3$. The radii of spheres follow a Gamma distribution with rate

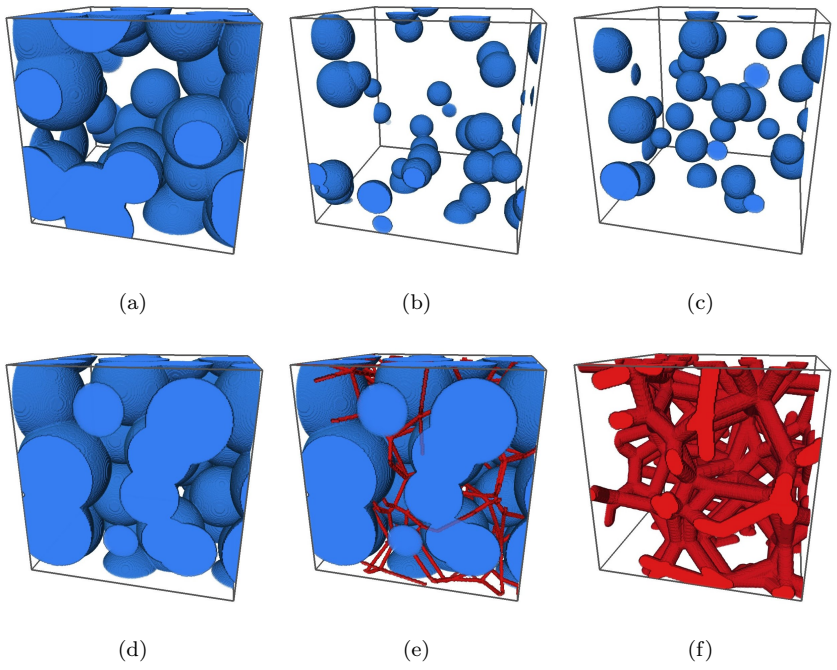

Figure 2: Overview of the modeling approach for a small example structure. (a) Initial sphere configuration. (b) Initital spheres with radii scaled by the core-shell ratio c. (c) Scaled spheres after applying the force-biased algorithm. (d) Spheres with radii scaled back to the original values. (e) Edges of the Laguerre tessellation generated by the spheres are shown in red. (f) System of dilated edges.

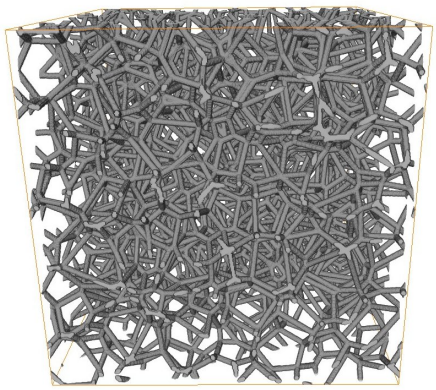

Figure 3: Simulated open-cell foam structure.

parameter 1 and shape parameter chosen such that, in expectation, there are 500 spheres in W when the packing density is reached. Finally, the dilation radius is chosen as $r = 308$ µm, which corresponds to 4.5 voxel, leading to porosities between 92.7% and 93.3% in our simulation outcomes. The parameter c is varied to generate structures with different morphological properties. This is discussed in Section 2.2.

Real open-cell foams do often not exhibit struts with a constant diameter, but the struts are thicker closer to their end points. This can be modeled using dilation with locally varying radii of spheres, see [20]. However, we restrict ourselves to the simple strut model with constant diameter, in order to keep the number of model parameters (and therewith the number of possible variables influencing morphological and functional properties) as small as possible. Nevertheless, to show that our analysis based on the simple strut model still leads to reasonable results, we modify three of our virtually generated structures such that struts are thicker at the end points, and compare their permeability with those of the original structures, see Section 5.

2.2. Generation of structures with different morphological properties

We make use of the stochastic microstructure model described in Section 2.1 to generate structures with different morphological properties. Remember that in recent studies the influence of the so-called coefficient of variation of cell volumes $\mathsf{cv}(V)$ has been investigated, where V is a random variable describing the volume of the (typical) cell in an open-cell foam, and

$$\mathsf{cv}(V) = \frac{\mathsf{sd}(V)}{\mathbb{E}(V)} \tag{2}$$

is the ratio between the standard deviation $\mathsf{sd}(V)$ and expectation $\mathbb{E}(V)$ of V. In the same manner we can define the coefficient of variation $\mathsf{cv}(A)$ for the area of the (typical) face A in an open-cell foam. It turns out that varying the core-shell ratio c leads to structures with rather different values of $\mathsf{cv}(A)$, while keeping $\mathsf{cv}(V)$ in a small range, thus allowing for a systematic analysis of the influence of $\mathsf{cv}(A)$. The different values of $\mathsf{cv}(A)$ in turn influence the so-

called constrictivity, which describes bottleneck effects in complex structures. It is defined as follows. Let $r_{\max}$ be the maximum radius such that 50% of the volume of the porous phase can be covered by (possibly overlapping) spheres with radius $r_{\max}$, which do not intersect with the solid phase. Furthermore, let $r_{\min}$ be the maximum radius such that 50% of the volume of the porous phase can be covered by spheres with radius $r_{\min}$ intruding from a pre-defined side of the material. For isotropic structures, the expectation of this (random) value is independent of the chosen direction. Note that the intrusion of spheres is limited on bottlenecks, and it holds $r_{\min} \leq r_{\max}$. Then the constrictivity β is defined via

$$\beta = \frac{r_{\min}^2}{r_{\max}^2}. \tag{3}$$

Obviously, $0 \leq \beta \leq 1$, and the smaller β is, the more and stronger bottleneck effects occur. A 2D sketch describing the meaning of $r_{\min}$ and $r_{\max}$ can be found in Figure 4. For more details, we refer to [23].

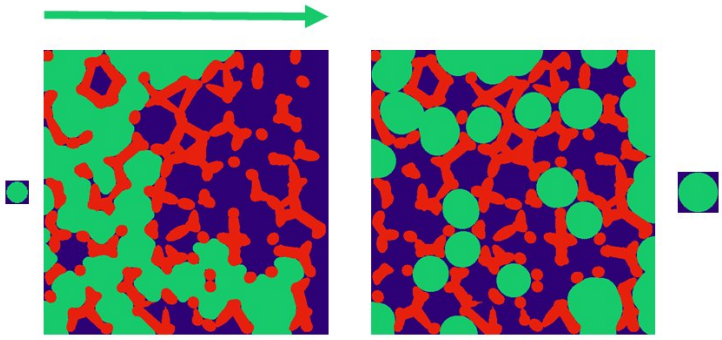

Figure 4: 2D sketch illustrating the definition of constrictivity. Left: The radius $r_{\min}$ is defined as the maximum radius for which 50% of the porous phase (blue) can be covered by spheres (which do not intersect with the complementary phase) intruding from the left side. All the parts of the porous phase that can be covered are shown in green color. Right: The radius $r_{\max}$ is defined as the maximum radius for which 50% of the porous phase can be covered by spheres (which do not intersect with the complementary phase) that are placed in the porous phase without having to intrude from a pre-defined side to their position.

We generated realizations of the model for five different core-shell ratios,

namely $c_1 = 0.3, c_2 = 0.475, c_3 = 0.65, c_4 = 0.825$ and $c_5 = 1$, with ten replications for each setting, resulting in a data base of 50 structures in total for the analysis of relationships between morphological and functional properties. The effect of the core-shell ratio on $\mathsf{cv}(A)$ is shown in Figure 5(a), where it can be clearly seen that with increasing core-shell ratio, the coefficient of variation of face sizes strongly decreases. Note that at the same time the coefficient of variation of cell volumes only varies between 0.4 and 0.48. For comparison, in [22], values between 0.48 and 2.08 have been studied in order to investigate the influence of $\mathsf{cv}(V)$ on permeability. Thus, the structures described above enable the analysis of the influence of $\mathsf{cv}(A)$ on permeability independently of $\mathsf{cv}(V)$.

In Figure 5(b), the relationship between $\mathsf{cv}(A)$ and constrictivity is shown, indicating a strong correlation. In the following analysis, we will consider the relationship between constrictivity and permeability, keeping in mind that, due to the strong correlation between constrictivity and $\mathsf{cv}(A)$, the results reflect the relationship between $\mathsf{cv}(A)$ and permeability. This choice is made because constrictivity is a normalized (between zero and one) aggregated morphological property, and it has turned out that functional properties of microstructures can even be described by empirical formulas that depend on, among others, constrictivity [17]. This provides the motivation to consider constrictivity as an explanatory variable when permeability is considered as the response variable in the following. Any relationship between constrictivity and permeability inherently shows a relationship between $\mathsf{cv}(A)$ and permeability.

2.3. Fluid flow calculations

ANSYS Fluent, Release 17.0 [31] is applied in order to determine permeability of the materials under consideration. The Navier-Stokes equations for the incompressible Newtonian fluid at steady state are solved in order to calculate pressure drop of fluid flowing through the structures under consideration. The flow across virtual and real structures was simulated with a computational domain channel of 50 mm length and 35mm x 35mm square cross section in accordance with real materials cross section. The size of the specimen was 35mm

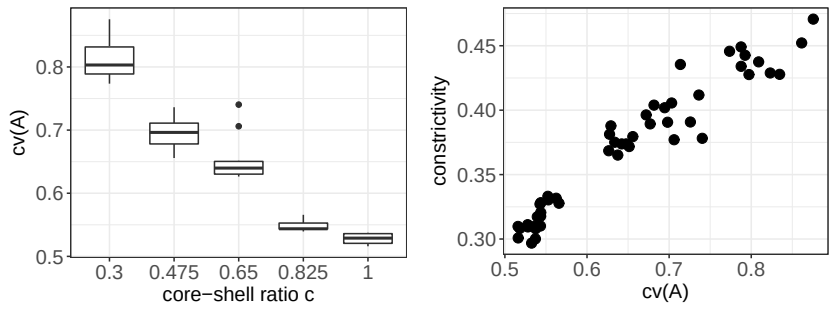

(a) (b)

Figure 5: Effect of core-shell ratio c on morphological properties. (a) Boxplot of $\mathsf{cv}(A)$ for model realizations with different core-shell ratios. The boxes show the regions between the 25%- and the 50%-quantiles, the line within each box shows the median value. Dots show outliers with a deviation of more than 1.5 times the interquartile distance to the median, vertical lines show the region from minimum to maximum value for each core-shell ratio (except for outliers). (b) Plot of constrictivity against $\mathsf{cv}(A)$.

x 35mm x 35mm. Boundary conditions are indicated in Figure 6. Walls of the channel and struts of the sample have no-slip 'wall' boundary conditions. The inlet velocity for FVM simulations was 10^{-5} m/s, which corresponds to a Reynolds number being equal to 0.35. Based on a mesh convergence study, a mesh size of around 12 million elements was found to be optimal for a proper description of the complex geometries of the samples. Experimental setup conditions have been applied as reference for the setup of the numerical model. Newtonian fluid flowing through the channel was water at room temperature. A more detailed description of the applied methodology can be found in [22]. The pressure drop value obtained from the numerical simulations can be applied by Darcy's equation to calculate permeability of the studied material, i.e.,

$$\frac{\Delta P}{\Delta L} = \frac{\mu u}{K u} \tag{4}$$

where ΔP is the obtained pressure drop [Pa], ΔL is the length of the sample [m], μ is the viscosity of the material [kg/ms], u is the velocity [m/s], and K is the permeability [m^2]. Darcy's law can be applied for flows with low Reynolds number (less than 1), where inertial effects are negligible [32].

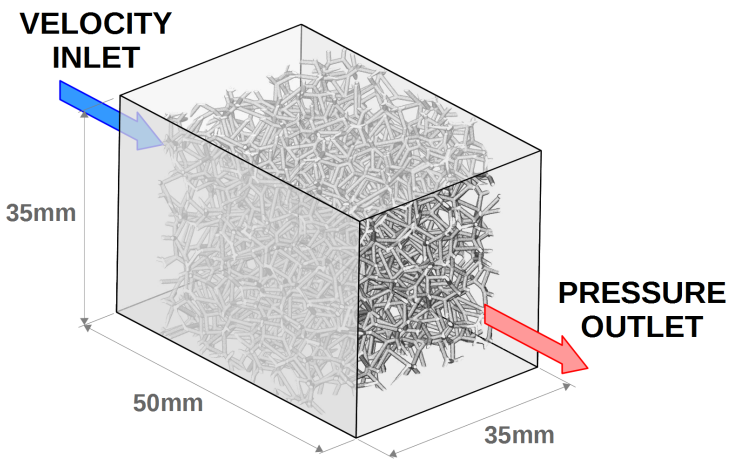

Figure 6: Computational domain with boundary conditions for permeability calculations of designed structures.

2.4. Selective laser melting

Three selected samples of the virtually designed porous foams were fabricated by the Realizer SLM-50 3D printer for metals and its alloys using titanium Grade 2 spherical powder (TLS Metal Powder GmbH, Leipzig, Germany). The average grain size of the powder was around $15 - 45$ µm while its purity was 99.7 wt.%. (0.11% Fe, 0.13% O, 0.01% C, 0.01% N, 0.001% H, balance Ti). The layer thickness was 50 µm, while the energy density used for powder consolidation was 45 J/mm^3 (scanning speed 375 mm/s and laser power 55 W). During fabrication, the building platform was heated to 200 °C to avoid thermal cracks and delamination. The argon inert atmosphere with a slight addition of oxygen (0.2 – 0.4 vol.%) to improve mechanical properties of fabricated structures was used [33]. Titanium foams were fabricated with support structures at the bottom and 3 mm from each side of the foam (Fig. 7(a)). The alternating laser scanning strategy with laser melting of boundaries and with 45° rotation of the

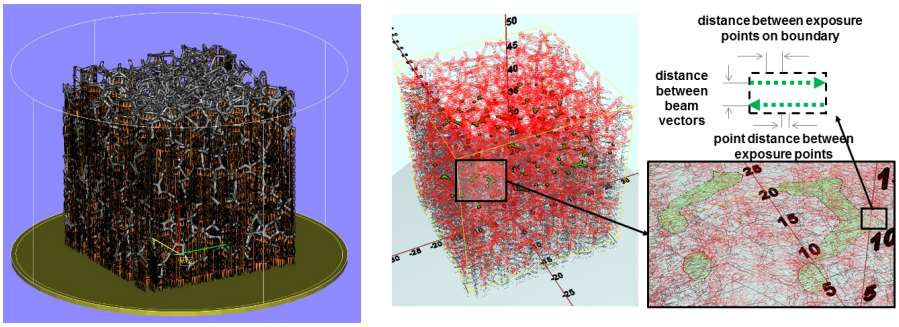

(a) (b)

Figure 7: Titanium foam with added support structures (a) and scheme of the laser scanning strategy used during SLM fabrication (b).

laser vector on each layer was used (Fig. 7(b)). Then, based on the sliced STL ("StereoLithography") foam model, which is a triangular representation of a 3-dimensional surface geometry, the first layer was selectively melted by a laser beam. After consolidation of the first layer the building platform was lowered by a predetermined thickness according to the designed structure and the next layer of the powder was distributed. The process of distributing powder, its selective melting by the laser beam and lowering of the table was repeated until the whole structure was fabricated.

2.5. Experimental pressure drop measurements

Experimental determination of permeability of chosen samples has been conducted using the set-up for pressure drop measurements, see Figure 8. In order to measure pressure drop the sample is placed in the test channel (see the zoom in Figure 8) and water is introduced. Note that the water is circulating in the closed system during the pressure drop measurement. The water flow rate in the test channel was regulated by valves and circulation pumps (90 Watts each). Filters and honeycomb flow straightener were installed in order to avoid fluctuations of fluid and sustain stable laminar flow during the measurement. Pressure difference is measured by sensors placed in front and behind the sam-

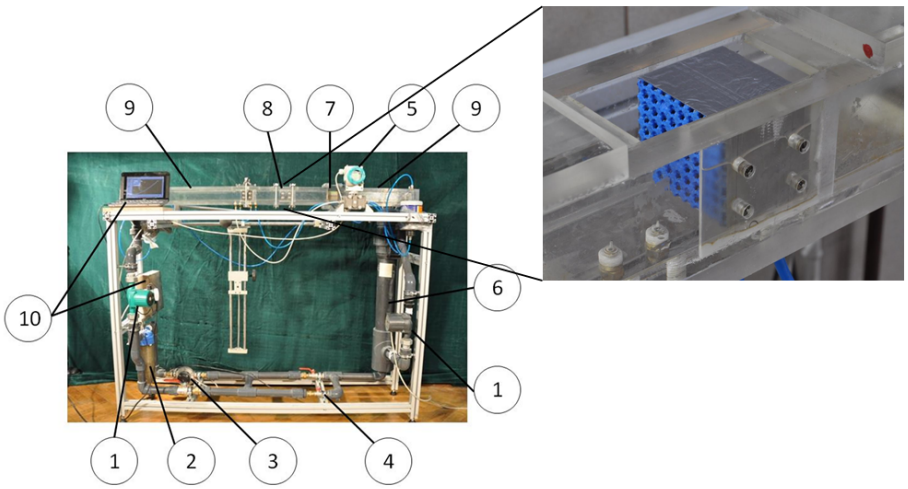

Figure 8: Experimental set-up for measuring pressure drop: Circulation pumps (1), water filter (2), oval wheel flowmeter with impulse output (3), gauge system (4), differential manometer Kobold DOM A20 with analog output (5), water container (6), honeycomb flow straightener (7), studied sample (8), auxiliary pneumatic vessels compensating for rapid pressure variations (9), digital data acquisition system (10). Addtionally, the zoom shows the mounting of the sample in the measurement channel.

ple. LabView software has been applied for data acquisition and control of the performed analysis. The pressure drop value for the given flow rate is obtained from the median of 20 measurements during 20 seconds (1 second each), which assures repeatable results. Pressure drop of water flowing through a channel has been measured for the designed structures. The working fluid was water at room temperature. Permeability of the materials was obtained using Darcy's equation (4).

3. Experimental validation

The method described in Section 2.3 enabled us to compute permeability for the set of structures with different morphological properties, which has been generated using the stochastic microstructure model based on Laguerre tessellations induced by sphere systems with different core-shell ratios, see Sections 2.1 and 2.2. In order to validate the results of the simulation procedure experimentally, three of the simulated structures have been selected for printing with SLM (as described in Section 2.4) and subsequent experimental analysis of pressure drop (as described in Section 2.5). Note that we selected structures with a rather different constrictivity (and therewith permeability), but rather similar porosity. An illustration showing a printed structure can be found in Figure 9. In Table 1, a comparison of simulated and experimentally gained values for permeability is shown. We find that the values obtained for permeability using simulation are slightly smaller than the ones gained experimentally. However, the difference is on average approximately 3% only. This shows that simulated and experimentally gained values are in good accordance with each other.

4. Results and discussion

The methods described in Section 2 provide a data basis of open-cell foams, their constrictivity, porosity and permeability. In Figure 10, the influence of constrictivity on permeability is shown. A certain correlation between constrictivity and permeability can be observed, although the variability is quite large

Figure 9: Printed open-cell foam structure using SLM.

	constrictivity	permeability [μm^2]		rel. difference
		simulated	experimental	
Structure 1	0.45	450923	461795	2.3%
Structure 2	0.37	428817	446623	4.0%
Structure 3	0.30	410417	423342	3.1%

Table 1: Comparison of simulated permeability with experimentally gained values.

and the correlation seems to level off for larger constrictivities. This is simply related with the fact that the porosities of the simulated structures slightly vary. Even though this variation is rather small, it has a huge impact, because porosity undoubtedly is the morphological characteristic with the highest influence on permeability. In order to show the effect of porosity, the data points in Figure 10 have been shaded according to their porosity. It turns out that the relationship between constrictivity and permeability can be described by a linear model, taking the porosity into account. Consider the formula

$$\kappa = \alpha_0 + \alpha_1 \beta + \alpha_2 p, \tag{5}$$

with κ being the permeability, β the constrictivity and p the porosity. Using the method of least squares leads to $\alpha_0 \approx -8.4 \cdot 10^6 \mu m^2, \alpha_1 \approx 2.8 \cdot 10^5 \mu m^2$ and $\alpha_2 \approx 9.4 \cdot 10^6 \mu m^2$ with an R-squared of more than 0.9. The coefficient of determination R-squared ranges from 0 to 1 and indicates the goodness-of-fit of the linear model, with values close to 1 indicating a good fit, see [34] for details. In order to illustrate the linear relationship between constrictivity and permeability for fixed porosity, according to Equation 5 three regression lines for fixed porosities have been added in the corresponding gray value in Figure 10. Note the good fit of data points with similar gray values as the corresponding regression lines, which supports the hypothesis of a linear relationship between constrictivity and permeability for fixed porosities. Additionally, a 3D plot of permeability against porosity and constrictivity, together with the fitted linear model, is shown in Figure 11.

Note that porosity is only included into the linear model because of its huge influence on permability, but that the range of porosity values that have been used to fit the linear model is rather small. Therefore, this relation might not be correct for porosities far away from these values. Thus, including porosity into the linear model is only a technical tool to show the linear relationship between constrictivity and permeability for fixed porosity. However, note that the stochastic model described in Section 2.1 can be used to generate structures for a broader range of porosities, which could then be used to derive more precise

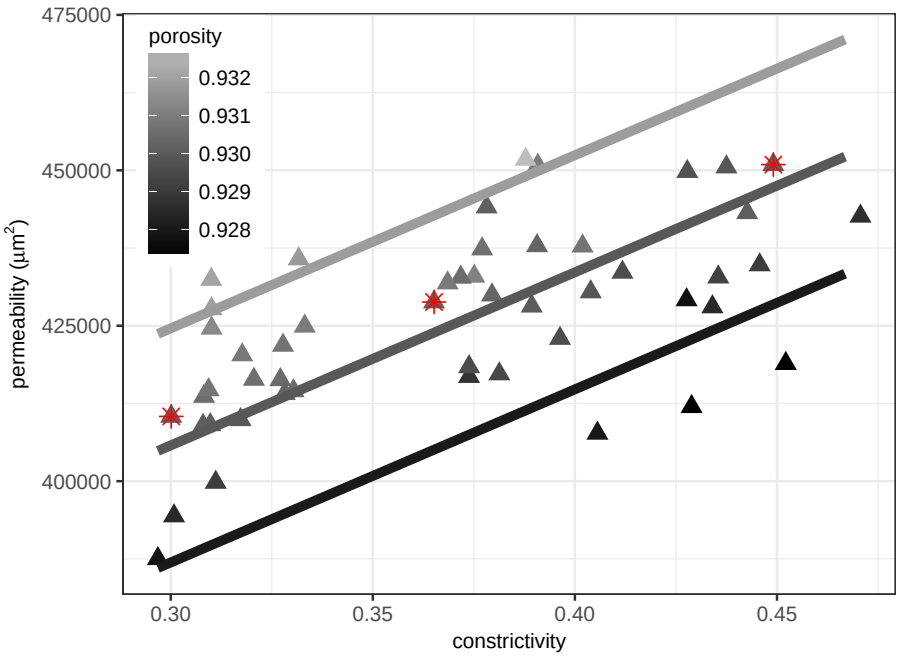

Figure 10: Relationship between constrictivity and permeability. Dots show results for the 50 simulated structures, lines indicate linear models for some fixed porosities. The gray values refer to the porosities of the corresponding structures. The red stars correspond to those structures that have been chosen for experimental validation.

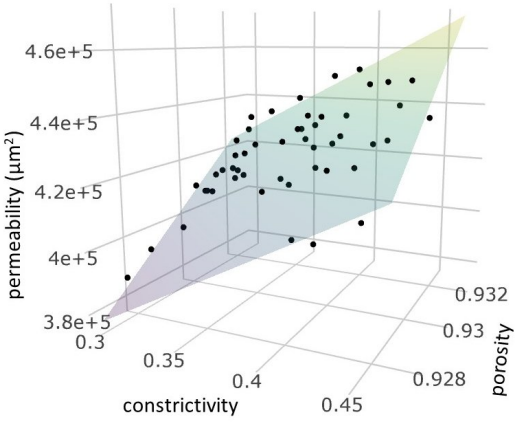

Figure 11: 3D plot showing the effect of constrictivity and porosity on permeability. Dots show the results for the 50 simulated structures. Additionally, a fitted linear model is shown.

empirical formulas. This procedure has succesfully been performed in [17] to derive an empirical formula expressing effective conductivity by volume fraction, constrictivity and tortuosity of microstructures related to fuel cells. Tortuosity, describing the ratio between shortest path length through a material to its thickness, is not very meaningful for the structures under consideration (as due to the very high porosity and the fact that the rather thin struts do not crucially disrupt transport paths, tortuosity is always very close to 1), but such a formula could for example be derived for the relationship expressing permeability by porosity, constrictivity and $\mathsf{cv}(V)$. However, this is beyond the scope of the present paper, where we introduce and validate the methodology and show that there is a linear relationship between constrictivity and permeability for fixed porosity.

To summarize, it turned out that the permeability of open-cell foams is strongly influenced by the constrictivity of their structure, which is, in turn, influenced by the distribution of face sizes. Moreover, it is shown that the relationship between permeability and constrictivity can be well described by a linear model when keeping other structural characteristics fixed.

5. Extension to different strut geometry

Recall that we have chosen to model the struts using tubes, in order to ensure that the results are not affected by the local geometry of more complex strut models. On the other hand, we also want to show that our results have a more general validity than only for the simple model with tube-shaped struts. In order to do so, we select three of the simulated structures (see red stars in Figure 10) and consider a modification of the strut model for them, keeping the positions and lengths of struts fixed but creating struts that are thicker on their endpoints.

The idea is as follows. We discretize each structure on the same voxel grid as before, but with a smaller strut diameter of approximately 100 µm, which corresponds to 1.5 voxels, resulting in a binary image I_{strut}, with $I_{\text{strut}}(v) = 1$ if

$v \in W$ belongs to the strut, and $I(v) = 0$ otherwise. Furthermore, we construct a second binary image I_{point} with $I_{\text{point}}(v) = 1$ if the voxel corresponding to $v \in W$ covers an endpoint of a strut. Then we consider the Euclidean distance map (see [35] for details) of both images, i.e.,

$$D_{\text{strut}}(v) = \min_{v' \colon I_{\text{strut}}(v')=1} ||v - v'|| \tag{6}$$

and

$$D_{\text{point}}(v) = \min_{v' \colon I_{\text{point}}(v')=1} ||v - v'|| \tag{7}$$

for each $v \in W$. Finally, we consider the image

$$D(v) = \begin{cases} 0, & \text{if } I_{\text{strut}}(v) = 1, \\ D_{\text{strut}}(v) + \delta D_{\text{point}}(v), & \text{otherwise,} \end{cases} \tag{8}$$

where it turned out that $\delta = 0.25$ leads to reasonable results. Then we define the image I of the advanced strut model via

$$I(v) = \begin{cases} 1, & \text{if } D(v) < t, \\ 0, & \text{otherwise,} \end{cases} \tag{9}$$

where the threshold $t \in \mathbb{R}_+$ is chosen such that the same porosity as for the original structure is achieved. Note that putting $D(v) = 0$ for each v with $I_{\text{strut}}(v) = 1$ ensures that no struts are disrupted, i.e., each strut that occurs in the simple strut model is also present in the advanced strut model, with a minimum diameter of 1.5 voxels (corresponding to approximately 100 µm). For a visual comparison of the simple and advanced strut models, see Figure 12.

We then compute the permeability of structures drawn from the more advanced strut model using the method described in Section 2.3. The results can be found in Figure 13. We observe a monotonous change of permeability, i.e., permeability increases when passing from structures drawn from the simple strut model to structures drawn fom the more advanced strut model, but the relationship between constrictivity and permeability is approximately retained. Thus, also for the advanced strut model, permeability increases with increasing

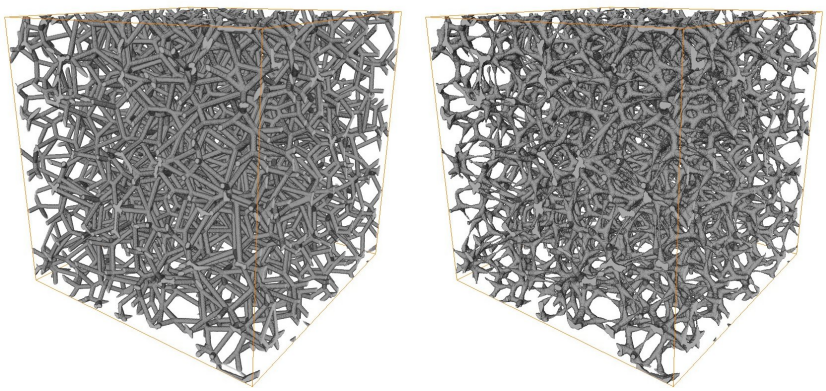

(a) (b)

Figure 12: Samples drawn from the (a) simple and (b) more complex strut model.

constrictivity. The red dashed line in Figure 13 indicates that a linear relationship between these two characteristics is still realistic. Thus, we can conclude that our findings are not only true for the simple strut model that we used, but can also be observed for more complex shapes of struts.

6. Conclusions

A stochastic microstructure model has been used to systematically generate virtual, but realistic open-cell foam structures with different coefficients of variation of face sizes. It was found that the face size distribution influences the constrictivity, which is a morphological characteristic describing bottleneck effects. The permeability of these virtual structures has been investigated using FVM, and the relationship between morphology and permeability has been investigated. An experimental validation of the results has been performed by using SLM to print three selected virtual structures and compare the results from real laboratory experiments to the ones gained by FVM. Moreover, it has been shown that the overall relationship between permeability and constrictivity is retained also for a more advanced strut model, rather than being true for the simple tube model only.

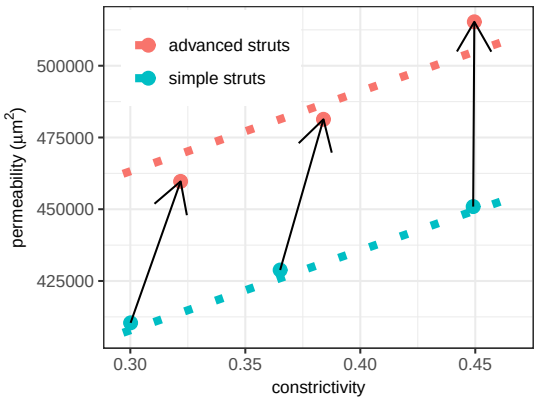

Figure 13: Comparison of computed permeabilities for the selected structures drawn from the simple and advanced strut model. The blue dashed line shows the permeability predicted by the linear model (5) for the average porosity of the three considered structures, the red dashed line is shifted by the mean difference in permeability between the simple and more advanced strut model.

It has been shown that for a given porosity and coefficient of variation of cell volumes, there is a linear relationship between the constrictivity and permeability. In addition, it is shown how the methodology of virtual materials testing can be used to derive empirical formulas for the relationship between morphological characteristics (e.g. porosity and constrictivity) and functional properties (e.g. permeability).

Data availability

The raw data required to reproduce these findings cannot be shared at this time as the data also forms part of an ongoing study. The processed data required to reproduce these findings are available to download from doi.org/10.18725/OPARU-5341.

References

[1] J. Adler, Ceramic diesel particulate filters, International Journal of Applied Ceramic Technology 2 (6) (2005) 429–439. doi:10.1111/j.1744-7402.

2005.02044.x.

[2] W. Azzi, W. Roberts, A. Rabiei, A study on pressure drop and heat transfer in open cell metal foams for jet engine applications, Materials & Design 28 (2) (2007) 569 – 574. doi:10.1016/j.matdes.2005.08.002.

[3] J. Richardson, Y. Peng, D. Remue, Properties of ceramic foam catalyst supports: pressure drop, Applied Catalysis A: General 204 (1) (2000) 19 – 32. doi:10.1016/S0926-860X(00)00508-1.

[4] L. Gibson, M. Ashby, Cellular Solids: Structure and Properties, Cambridge Solid State Science Series, Cambridge University Press, Cambridge, 1999.

[5] E. A. Moreira, J. R. Coury, The influence of structural parameters on the permeability of ceramic foams, Brazilian Journal of Chemical Engineering 21 (2004) 23 – 33. doi:10.1590/S0104-66322004000100004.

[6] S. Mancin, C. Zilio, A. Cavallini, L. Rossetto, Pressure drop during air flow in aluminum foams, International Journal of Heat and Mass Transfer 53 (15–16) (2010) 3121 – 3130. doi:10.1016/j.ijheatmasstransfer.2010.03.015.

[7] N. Dukhan, Correlations for the pressure drop for flow through metal foam, Experiments in Fluids 41 (4) (2006) 665–672. doi:10.1007/s00348-006-0194-x.

[8] G. I. Garrido, F. Patcas, S. Lang, B. Kraushaar-Czarnetzki, Mass transfer and pressure drop in ceramic foams: A description for different pore sizes and porosities, Chemical Engineering Science 63 (21) (2008) 5202 – 5217. doi:10.1016/j.ces.2008.06.015.

[9] D. L. Johnson, J. Koplik, R. Dashen, Theory of dynamic permeability and tortuosity in fluid-saturated porous media, Journal of Fluid Mechanics 176 (1987) 379–402. doi:10.1017/S0022112087000727.

[10] C. Perrot, F. Chevillotte, R. Panneton, Bottom-up approach for microstructure optimization of sound absorbing materials, The Journal of the Acoustical Society of America 124 (2) (2008) 940–948. doi:10.1121/1.2945115.

[11] F. Chevillotte, C. Perrot, Effect of the three-dimensional microstructure on the sound absorption of foams: A parametric study, The Journal of the Acoustical Society of America 142 (2) (2017) 1130–1140. doi:10.1121/1.4999058.

[12] P. Ranut, On the effective thermal conductivity of aluminum metal foams: Review and improvement of the available empirical and analytical models, Applied Thermal Engineering 101 (2016) 496–524. doi:10.1016/j.applthermaleng.2015.09.094.

[13] P. Kumar, F. Topin, State-of-the-art of pressure drop in open-cell porous foams: Review of experiments and correlations, Journal of Fluids Engineering 139 (11) (2017) 111401. doi:10.1115/1.4037034.

[14] K. K. Bodla, J. Y. Murthy, S. V. Garimella, Microtomography-based simulation of transport through open-cell metal foams, Numerical Heat Transfer, Part A: Applications 58 (7) (2010) 527–544. doi:10.1080/10407782.2010.511987.

[15] S. H. Ibrahim, M. Neumann, F. Klingner, V. Schmidt, T. Wejrzanowski, Analysis of the 3D microstructure of tape-cast open-porous materials via a combination of experiments and modeling, Materials & Design 133 (2017) 216 – 223. doi:10.1016/j.matdes.2017.07.058.

[16] M. Neumann, J. Staněk, O. M. Pecho, L. Holzer, V. Beneš, V. Schmidt, Stochastic 3D modeling of complex three-phase microstructures in SOFC-electrodes with completely connected phases, Computational Materials Science 118 (2016) 353–364.

[17] O. Stenzel, O. Pecho, L. Holzer, M. Neumann, V. Schmidt, Big data for microstructure-property relationships: A case study of predicting effective

conductivities, AIChE Journal 63 (2017) 4224–4232. doi:10.1002/aic.15757.

[18] C. Redenbach, Microstructure models for cellular materials, Computational Materials Science 44 (4) (2009) 1397 – 1407. doi:10.1016/j.commatsci.2008.09.018.

[19] A. Liebscher, H. Andrä, M. Kabel, D. Merkert, C. Redenbach, Modelling open cell foams based on 3D image data, in: Proceedings of the 20th International Conference on Composite Materials, Copenhagen, 2015.

[20] C. Lautensack, M. Giertzsch, M. Godehardt, K. Schladitz, Modelling a ceramic foam using locally adaptable morphology, Journal of Microscopy 230 (3) (2008) 396–404. doi:10.1111/j.1365-2818.2008.01998.x.

[21] C. Redenbach, I. Shklyar, H. Andrä, Laguerre tessellations for elastic stiffness simulations of closed foams with strongly varying cell sizes, International Journal of Engineering Science 50 (1) (2012) 70–78.

[22] J. Skibinski, K. Cwieka, T. Kowalkowski, B. Wysocki, T. Wejrzanowski, K. J. Kurzydlowski, The influence of pore size variation on the pressure drop in open-cell foams, Materials & Design 87 (2015) 650 – 655. doi:10.1016/j.matdes.2015.08.079.

[23] L. Holzer, D. Wiedenmann, B. Münch, L. Keller, M. Prestat, P. Gasser, I. Robertson, B. Grobéty, The influence of constrictivity on the effective transport properties of porous layers in electrolysis and fuel cells, Journal of Materials Science 48 (7) (2013) 2934–2952. doi:10.1007/s10853-012-6968-z.

[24] B. Wysocki, P. Maj, R. Sitek, J. Buhagiar, K. J. Kurzydłowski, W. Święszkowski, Laser and electron beam additive manufacturing methods of fabricating titanium bone implants, Applied Sciences 7 (7) (2017) 657. doi:10.3390/app7070657.

[25] S. Torquato, Random Heterogeneous Materials, Springer, New York, 2013.

[26] C. Lautensack, Random Laguerre Tessellations, Ph.D. thesis, Karlsruhe Institute of Technology (2007).

[27] S. N. Chiu, D. Stoyan, W. S. Kendall, J. Mecke, Stochastic Geometry and its Applications, 3rd Edition, J. Wiley & Sons, Chichester, 2013.

[28] J. Mościński, M. Bargieł, Z. A. Rycerz, P. W. M. Jacobs, The force-biased algorithm for the irregular close packing of equal hard spheres, Molecular Simulation 3 (1989) 201–212. doi:10.1080/08927028908031373.

[29] A. Bezrukov, M. Bargieł, D. Stoyan, Statistical analysis of simulated random packings of spheres, Particle & Particle Systems Characterization 19 (2) (2002) 111–118. doi:10.1002/1521-4117(200205)19:2<111::AID-PPSC111>3.0.CO;2-M.

[30] A. Spettl, R. Wimmer, T. Werz, H. Heinze, S. Odenbach, C. E. Krill, V. Schmidt, Stochastic 3D modeling of Ostwald ripening at ultra-high volume fractions of the coarsening phase, Modelling and Simulation in Materials Science and Engineering 23 (2015) 065001. doi:10.1088/0965-0393/23/6/065001.

[31] ANSYS® Fluent, Relase 17.0, Help System, Theory Guide, ANSYS, Inc.

[32] W.Sobieski, A.Trykozko, Darcy's and Forchheimer's laws in practice. Part 1. The experiment, Technical Sciences 17 (4) (2014) 321–335. doi:10.1121/1.2945115.

[33] B. Wysocki, P. Maj, A. Krawczyńska, K. Rożniatowski, J. Zdunek, K. J. Kurzydłowski, W. Święszkowski, Microstructure and mechanical properties investigation of CP titanium processed by selective laser melting (SLM), Journal of Materials Processing Technology 241 (2017) 13 – 23. doi:10.1016/j.jmatprotec.2016.10.022.

[34] B. J. Chalmer, Understanding Statistics, Marcel Dekker Inc., New York, 1987.

[35] P. F. Felzenszwalb, D. P. Huttenlocher, Distance transforms of sampled functions, Theory of Computing 8 (2012) 415–428.